PCCP

ROYAL SOCIETY OF CHEMISTRY

PAPER

View Article Online
View Journal

Cite this: DOI: 10.1039/d5cp03788c

Libration of hydroxyl groups in layered aluminum (oxy)hydroxides and other material analogs: insights from inelastic neutron scattering and theory

Hsiu-Wen Wang, *[a] Micah P. Prange, *[b] Trent R. Graham, [b] Xin Zhang, [b] Tingting Liu, [a] Luke Daemen,[c] Alexander I. Kolesnikov, [c] Gregory K. Schenter, [b] Lawrence M. Anovitz, [a] Kevin M. Rosso [b] and Carolyn I. Pearce [bd]

Received 30th September 2025,
Accepted 19th November 2025

DOI: 10.1039/d5cp03788c

rsc.li/pccp

We analyzed the hydroxyl librational signatures of five structurally related aluminum (oxy)hydroxides, using inelastic neutron scattering (INS) and plane-wave lattice dynamics simulations. A clear trend across these aluminum-containing phases illustrates the relationship between hydrogen bonding, local atomic structure, and the spectral location and profile of the librational bands. The INS spectra have been compared to previous optical spectroscopy and computational studies, highlighting the complementary nature of the INS technique. Taking into account other structurally or chemically related material analogs, we have identified a correlation between a blueshift (to higher energy) of the upper librational band edge and the geometry of the hydrogen bond interactions, mirroring (with opposite correlation) the well-known redshift in the intramolecular O–H stretching energy with increasing hydrogen bond strength. For hydroxyl groups that do not participate in hydrogen bonding effectively, the bending librations occur at lower energies and hybridize with metal–oxygen lattice modes. Standard density functional theory approximations, including dispersion corrections, struggle to correctly predict vibrational frequencies of motions dominated by H but perform well for metal–oxygen modes, allowing us to make detailed mode assignments in several cases, including a demonstration of how layer-to-layer disorder in boehmite hydrogen bond orientations is reflected in the sharp but minor low energy peaks (at ~70–80 meV) of the INS spectrum.

1. Introduction

Interest in hydroxyl group motions within oxide crystal lattices dates back to the middle of the last century.[1–5] The strength of hydrogen bonds (HBs), the relevant proton motions (vibration and libration), and the degree of mechanical coupling to the low-frequency lattice dynamics (phonons) influence many aspects of structural stability and behavior,[6–8] such as (de)hydration, dissolution, and phase transformations. The study of proton dynamics is of particular interest in the context of HB networks in 3-dimensional frameworks (*e.g.*, hydrated salts and zeolites) and 2-dimensional materials (*e.g.*, phyllosilicate clays, metal hydroxides, and engineered layered compounds), because part of the H motions mirror the dynamics of the entire structure, reflecting the long-range order and many properties of the solids.[1,7,8] For example, the number, symmetries, and energies of the phonon modes are related to the material's dielectric properties and specific heat.[9]

Vibrational spectroscopy by inelastic neutron scattering (INS) is a well-established technique for probing H atom dynamics over a wide range of energy transfers (~0–500 meV; ~0–4000 cm^{-1}). The incoherent scattering cross-section of H is by far the largest compared to that of other elements typically present in a compound and is also far greater than the coherent cross-sections of both H and all other elements. Thus, the most intense signatures are those associated with the H dynamics, making INS the ideal technique for studying hydroxyl or molecular water groups.[7,10,11] Furthermore, symmetry-related selection rules do not apply to the INS spectra, so all modes should be observed.[7,10] These key features distinguish INS from infrared (IR) or Raman spectra, where (in the latter cases) the optical spectra in a similar energy transfer region (<150 meV; <1200 cm^{-1}) are dominated

[a] *Chemical Sciences Division, Oak Ridge National Laboratory, Oak Ridge, Tennessee 37831, USA. E-mail: wanghswen@gmail.com*
[b] *Pacific Northwest National Laboratory, Richland, Washington 99354, USA. E-mail: Micah.Prange@pnnl.gov*
[c] *Neutron Scattering Division, Oak Ridge National Laboratory, Oak Ridge, Tennessee 37831, USA*
[d] *Department of Crop and Soil Sciences, Washington State University, Pullman, Washington 99164, USA*

by the strong stretching/deformation modes of bonds involving "heavy" atoms, forming the main structure. In addition, because the intensities of dynamic modes observed in INS are related to the mean square displacements of the scattering atoms, they can be directly compared with the calculated vibrational density of states (VDOS) through a Fourier transform of the velocity autocorrelation functions or diagonalization of the dynamical matrix. As VDOS calculations are routinely performed using density functional theory (DFT),[12] integration of DFT with all three forms of vibrational spectroscopy (IR, Raman and INS) can result in unambiguous mode assignments in both transition energies and relative intensities.[13]

Here, we show that the INS data can be used to observe all the vibrational motions below the O–H stretching bands in common H-bearing minerals. The INS spectra are presented for a selection of structurally related aluminum minerals, including oxyhydroxide AlO(OH) (diaspore and boehmite), hydroxide $Al(OH)_3$ (gibbsite and bayerite), and hydroxyl intercalated lithium–aluminum-layered double hydroxide $Li[Al(OH)_3]_2{\cdot}OH{\cdot}2H_2O$ (in short, OH-LiAl-LDH). All consist of close-packed oxygen networks forming octahedral interstices occupied by Al^{3+} and contain various hydroxyl groups to ensure HB cross-linkages and cohesion of the layered AlO(OH) or $Al(OH)_3$ building blocks.[14–18] In the OH-LiAl-LDH structure, the Li^+ ion is located in vacant $Al(OH)_3$ octahedral sites, forming a positively charged $Li[Al(OH)_3]_2^+$ layer unit, which is neutralized by intercalation of OH^- ions and water molecules between layers.[18] All except OH-LiAl-LDH have been extensively characterized by both IR and Raman spectroscopy (diaspore,[19–24] boehmite,[19–22,25–27] gibbsite,[16,19–22,28,29] and bayerite[19–21,28,30]). Detailed symmetry group analysis, together with DFT simulations, has also been used to explain, for example, the spectral structure of the O–H stretches at the Brillouin zone center due to mode coupling or anisotropic particle size effects.[23–25,28] The aim of this study is to provide a brief review and a more complete analysis of vibrational dynamics in these phases by means of INS spectroscopy. DFT calculations were used for mode assignments. Although they work well for this purpose, comparison of the calculated vibrational spectra with the observed INS vibrations confirms that standard dispersion corrections to the exchange–correlation potential (*e.g.* Grimme D3) are insufficient to accurately predict H bending energies.

This study focuses on the low- and middle-energy ranges ($\sim$5–200 meV; $\sim$40–1600 cm^{-1}), where libration and lattice translation involving proton motions occur. Such INS spectra are complementary to the optical spectra, because the intensities of the modes associated with aluminum (Al) and oxygen (O) in the optical spectra are intense, masking the weaker proton motions. After analysis of the INS spectra using calculated VDOS, we compared the INS to the available IR and Raman vibrational modes to distinguish, for example, the hydroxyl bending librations from the deformation of non-hydrogenous Al–O units. Additionally, since H atom librational dynamics are very sensitive to the local bonding environment, a comparison between these samples and published INS data on analogous materials permits the establishment of generalized correlations between the hydroxyl bending modes and the strength/geometry of HB interactions. The structurally or chemically related phases include: ferric oxyhydroxides FeO(OH) (goethite and lepidocrocite), phyllosilicate clays (kaolinite, muscovite and phlogopite), various layered metal hydroxides (theophrastite–$Ni(OH)_2$, brucite–$Mg(OH)_2$, portlandite–$Ca(OH)_2$, and LiOH-II), and alkaline aluminate salts ($K_2[Al_2O(OH)_6]$, $Rb_2[Al_2O(OH)_6]$, and $Cs[Al(OH)_4]{\cdot}2H_2O$).

2. Experimental methods

2.1 Material descriptions and synthesis

A gem quality diaspore sample was obtained from Pinarcik, Mugla, Turkey.[31] A small piece of this mineral was ground into micro-sized powders for the INS experiment. Boehmite, gibbsite, and bayerite samples were synthesized *via* hydrothermal alteration of an amorphous aluminum hydroxide precursor, following our established method.[32,33] Briefly, the amorphous aluminum hydroxide precursor was prepared from a 0.25 M aqueous solution of aluminum nitrate ($Al(NO_3)_3$) and the pH was adjusted by the addition of concentrated sodium hydroxide (NaOH) solution. Different pHs are required for the synthesis of each phase: the precursor for boehmite synthesis requires a pH of $\sim$10, and the precursor for gibbsite and bayerite syntheses requires a pH of $\sim$5. The amorphous precursor precipitates were then collected and redispersed in deionized (DI) water for hydrothermal treatment. For OH-LiAl-LDH synthesis,[18] the synthesized gibbsite powders were dried and used as a precursor by redispersing the powders into concentrated lithium hydroxide (LiOH) solution for a week-long dissolution–reprecipitation reaction. Detailed descriptions of the synthesis of each phase are provided in the SI.

2.2 Inelastic neutron scattering (INS) measurements

The INS spectra were collected on the VISION instrument at the Spallation Neutron Source at the Oak Ridge National Laboratory. VISION is an inverse geometry time-of-flight neutron spectrometer, equipped with arrays of pyrolytic graphite analyzer and Be-filters to provide an improved signal-to-noise ratio and good energy transfer resolution over a broad energy range.[34] Inverse geometry means that the final momentum and energy of the scattered neutrons are fixed while the momentum and energy of the incident neutrons vary as a function of time. In VISION, only two fixed trajectories in the momentum and energy transfer Q-E space are tracked by the two detector banks.[34] This design means that VISION provides good energy resolution (1–2%) and spectral statistics at low- to mid-range energy transfers ($<\sim$200 meV). In the high-energy region, however, the intensity of the INS spectra is significantly attenuated by the Debye–Waller factor and is submerged in a multi-phonon contribution due to large neutron momentum transfers.[35] Therefore, the high energy intramolecular O–H stretching modes, for example, appear as broad/indistinct bands, and usually only their presence or absence is reported. To overcome the INS resolution limits for high energy vibrational modes, a direct geometry instrument, such as SEQUOIA, is a better choice. The INS data were collected on the five samples mentioned in the previous section. Approximately 1 g of each powder sample was transferred to a He glove box and loaded into a 10 mm

cylindrical vanadium can. The sample can was mounted inside a cryostat and cooled to 15 K to collect the spectrum. The generalized vibrational densities of states G(E) were constructed from the experimental data using MANTID.[36] The background spectra measured with no sample present provided scattering data from the sample holder and cryostat. We utilized the VISION data to characterize vibrations of H-bonded network signatures in the samples. Complementary neutron diffraction patterns were also extracted to provide a quality check on the samples (Fig. S1).

2.3 Simulation and vibrational density of states (VDOS) calculation

We performed frozen phonon lattice dynamics calculations using the Vienna *ab initio* simulation package (VASP[37]) and phonopy[38] packages. The PBE exchange correlation approximation[39] was used with and without D3[40,41] dispersion corrections. An energy cutoff of 750 eV was employed for all calculations, which were done within the projector-augmented wave methodology[42] using standard VASP datasets exposing 3, 6, and 1 valence electrons for Al, O, and H atoms, respectively. Initial structures were taken from the literature for diaspore,[43] boehmite,[44] gibbsite,[45] and bayerite.[46] *K*-point grids for relaxations were Γ-centered of size $8 \times 3 \times 12$, $12 \times 2 \times 9$, $4 \times 7 \times 3$, and $3 \times 2 \times 3$ for diaspore, boehmite, gibbsite, and bayerite, respectively. All lattice and internal coordinates were relaxed. To calculate the force constants, central differences were constructed by displacing single atoms by 0.01 Å in the supercells. The dimensions of the supercells (*k*-grid) were $3 \times 1 \times 3$ ($2 \times 3 \times 4$), $3 \times 1 \times 3$ ($4 \times 2 \times 3$), $1 \times 2 \times 2$ ($3 \times 2 \times 3$), and $2 \times 1 \times 2$ ($3 \times 2 \times 3$) for diaspore, boehmite, gibbsite, and bayerite, respectively.

3. Results and discussion

3.1 General description of hydroxyl librations and translations

When a hydroxyl group is bound to a metal ion in a coordination complex, two types of hydroxyl librations can be observed by INS in the energy range of this study: the Al–O–H bending and riding motions. The Al–O–H bending mode considers the relative rotational oscillations of the H atom with respect to its covalently bonded O atom, *i.e.*, the motions of the H atom perpendicular to the covalent O–H bond axis (bending movement is also called wagging movement). This movement incorporates a great H displacement and is primarily responsible for features in the librational fingerprint region. The bending movements should not, however, be confused with the fundamental O–H bond stretching modes, which occur at a higher energy (above ~300 meV; ~2400 cm^{-1}). In isolation, the H atom in a linear (O–H···O) motif will exhibit a single stretching and doubly degenerate bending vibration. In a hydrogen-bonded crystalline material, additional dispersion is introduced by the crystal field at the H site, which can split the double degeneracy of the isolated bends and couple vibrations at different H sites. Consequently, band structure effects generate different vibrational energies for relative phases of motion at adjacent sites described by different wavevectors in the Brillouin zone of the crystal. For example, if the (O–H···O) lies in a crystal symmetry plane (as in diaspore and boehmite), the bending movements can be decomposed into the in-plane and the out-of-plane branches with the degree of dispersion depending on whether the motions bring two nearby H atoms close to each other or not.[23–25] This results in the usual order of the stiffer in-plane mode having higher energies than the out-of-plane modes.[4] These band structure effects are observable by INS, which is not limited to optically active modes at the zone center.

The riding mode is a whole-body (rigid) hydroxyl group movement modulated by, *e.g.*, Al–O bond stretching, AlO_6 octahedra deformation, or wobbling of the octahedra layered units. These movements cause a smaller H displacement, and, owing to the larger mass of Al and O compared to H, occur at lower energies. We show that these motions can be observed by INS in some cases. The riding mode can be viewed as characteristic of hydroxyl groups tightly bound to a metal center and appears in a relatively wide energy range due to the strong dispersion of various octahedral deformation modes. In the context of molecular crystals, where many vibrations can be correlated with internal vibrational modes of a gas phase molecule, the term translational mode is used to describe rigid (*i.e.* riding) external translations of the molecule within the crystal. This term is, however, more commonly used to generically describe a cluster of overlapping low-intensity INS peaks extending from the elastic line (at zero energy transfer) to about 50 meV (400 cm^{-1}), due to sublattice oscillations and collective motions in hydrogen-bonded crystals.

As noted above, the signal observed by VISION in the O–H stretching region is strongly suppressed by the Debye–Waller effect and a large background of overtones and combinations. Thus, the INS spectra from this instrument do not have well resolved peaks in the high energy region, where O–H stretching vibrations should be detected. Thus, these are only mentioned briefly for each mineral. Nevertheless, using theoretical lattice dynamics, we show that the stretching and bending frequencies are strongly correlated and that inferences about the stretches can be drawn from the librational band shape, which is well resolved by VISION.

Fig. 1 shows the INS spectra of the five measured mineral samples in the librational and translational fingerprint region. The spectra are arranged in the order of structural complexity, corresponding to the spectral positions of the stiffest librational bands. Comparing diaspore and OH-LiAl-LDH, which can be regarded as end-members, diaspore has a relatively "simple fingerprint" as it only contains one type of hydroxyl group located in the AlO_6-strip tunnel spaces. In contrast, the "complex fingerprint" of OH-LiAl-LDH arises from the coexistence of multiple HB configurations, introduced by intercalated hydroxide (OH^-) and water (H_2O) species, which form HBs with each other and with the layer hydroxyl groups. Boehmite also possesses a single H site, but its librational band profile is wider and more complicated due to stronger coupling between the motion of neighboring H atoms.

3.2 Diaspore

The structure of diaspore (α-AlO(OH)) is based upon a hexagonal-close-packed array of oxygens. The AlO_6 octahedra

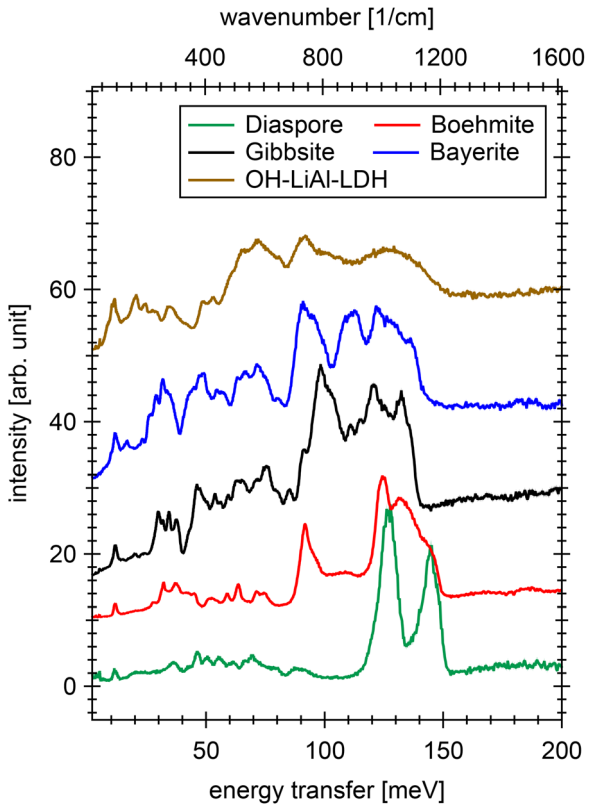

Fig. 1 INS spectra of diaspore, boehmite, gibbsite, bayerite and OH-LiAL-LDH, arranged in the order of increasing structural complexity (from bottom to top) and in the order of shifting the overall librational bands from the high-to-low energy transfers. The energy units are in both meV and cm^{-1}, where 1 meV = 8.065 cm^{-1}. The lowest peak observed at 12 meV is an artifact of the VISION spectrometer and is presented in all five studied samples; see the SI for details.

are linked *via* edge-sharing to form strips in the *z* direction.[14] The AlO_6-strip packing creates tunnel spaces containing HBs, and, strictly speaking, diaspore is a non-layered material (Fig. S2a), despite its perfect cleavage. The structure contains four symmetry-equivalent AlO(OH) units per unit cell. As shown in Fig. 2(a), the four irreducible atoms (Al, O, and OH group) lie on the mirror plane (the *xy* plane). Each O atom is tetrahedrally coordinated by three Al atoms and the fourth is coordinated to a H atom, either covalently (as a μ_3-OH group; HB donor) or *via* hydrogen bonds (as a μ_3-O atom; HB acceptor). The geometric definition of Luzar and Chandler[47] was used to categorize the HB configurations. Descriptions on the length and angle relationships are given in Table 1. Factor group analysis and detailed mode assignments have been performed for the IR and Raman spectra of diaspore.[23,24] Fig. 2(b), which compares the INS spectrum with the experimentally observed IR and Raman transitions,[19–24] shows that the INS data are consistent with the expected IR- and Raman-active bands in the fingerprint region. In the 110–150 meV region, the 145 meV in-plane (movement in the *xy* plane) and the 126 meV out-of-plane (movement normal to the *xy* plane) Al–O–H bending modes generate strong, narrow INS bands that are well-separated from the lattice deformation modes appearing under 110 meV. The Al–O–H bending band is about 40 meV wide, indicating some coupling among the four hydroxyl groups in the unit cell. The Al–O–H bending modes have low intensity spectral signatures in the powder IR or Raman spectra.[19–24] The light blue tick marks in Fig. 2(b) represent polarized single-crystal Raman measurements obtained using a gem quality diaspore sample with better resolved Raman bands.[24] In the 15–110 meV region, a series of hydroxyl riding/translational modes was observed. Their low intensities confirm that these modes are associated with various lattice deformations (distortions or relative displacements of AlO_6 octahedra), in accordance with our theoretical predictions (Fig. S4).

Two different mode assignments have been proposed for the IR band at ~120 meV based on the frequency similarity between experiments and simulations: (i) a pure Al–O–H bending mode; or (ii) an overtone band involving AlO_6 subunits.[23,24]

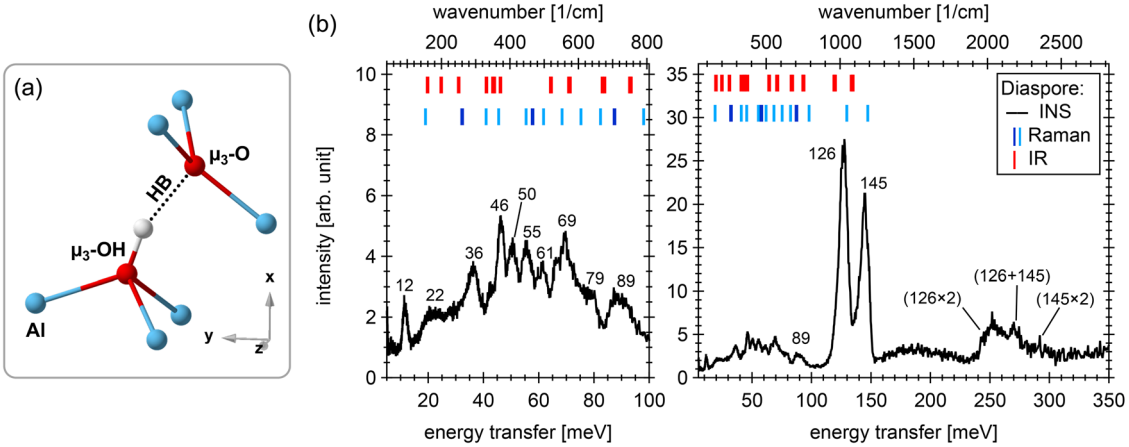

Fig. 2 (a) Local hydrogen bond (HB) environment in diaspore. Al, O and H atoms are represented in blue, red and white spheres, respectively. Fourfold coordination for the μ_3-OH group and μ_3-O atom is emphasized; see Fig. S2a for a complete diaspore structure.[14] (b) INS spectrum of diaspore and its comparison to the experimental Raman and IR data from the literature.[19–24] For simplicity, tick marks are used to label transitions observed by optical spectroscopy (only strong-medium intensity IR/Raman bands are marked). The number labels indicate the energy transfers of the most relevant features in meV. The 12 meV peak is an artifact of the VISION spectrometer.

Table 1 Geometry of the O–H···O hydrogen bonds (HBs) in various Al^{3+}-containing materials. According to the geometric definition,[47] a HB exists when the interoxygen distance (O···O) is less than 3.5 Å, and simultaneously, the angle between the O–H axis and the interoxygen axis (∢H–O···O) is smaller than 30°. A zero angle of ∢H–O···O represents a linear HB geometry

Phase	H···O (Å)	O···O (Å)	∢H–O···O (°)	HB strength[a]
Diaspore (*Pbnm*; no. 62)[14]				
Network O2–H···O1	1.692	2.651	11.88	Moderate
Boehmite ($Cmc2_1$; no. 36)[15]				
Interlayer O2–H···O2	1.814	2.733	8.40	Moderate
Gibbsite ($P2_1/n$; no. 14)[16]				
Interlayer O1–H1···O4	1.849	2.825	9.36	Moderate
Interlayer O2–H2···O6	1.816	2.792	5.63	Moderate
Interlayer O3–H3···O5	1.930	2.899	9.91	Moderate
Intralayer O4–H4···O3	2.033	2.971	13.62	Moderate
Intralayer O5–H5···O1	2.237	3.058	28.20	Weak
Intralayer O6–H6···O3	2.212	3.109	19.91	Weak
Bayerite ($P2_1/n$; no. 14)[17]				
Interlayer O1–H1···O4	1.927	2.890	1.83	Moderate
Interlayer O2–H2···O6	2.005	2.996	11.99	Moderate
Interlayer O3–H3···O5	2.028	2.965	6.86	Moderate
Intralayer O4–H4···O2	2.106	3.028	18.48	Moderate
Intralayer O5–H5···O1	2.276	3.043	29.75	Weak
Intralayer O6–H6···O2	2.433	3.219	30.18	Weak

[a] The strong, moderate and weak definitions of the HBs are based on descriptions by Jeffrey.[59] The graphical representation of HB length, enthalpy and the redshift of the O–H stretching energy is illustrated by Wang *et al.*[11]

Since there is a clear gap in the INS spectrum at about 110 meV, where the scattered energy drops to the background level (Fig. 2(b)), the reported IR peak at ∼120 meV, which lies in the bending mode region, should be interpreted as a bending movement. From its position near the bottom of the 126 meV INS peak, and comparison to phonon band structure calculations, we conclude that it should belong to the B_1 irreducible representation of diaspore's D_{2h} point group symmetry. This unambiguous assignment illustrates the value of measuring the full vibrational spectrum using INS, compared to just the zone center vibrations accessible to optical spectroscopy.

Other features of the INS spectrum, *e.g.*, the two broad bands in the 150–340 meV region (Fig. 2(b)), are not discussed because these bands, which are absent in the normal mode analysis, correspond to combinations of hydroxyl bending and riding modes (centered at ∼180 meV), or overtones of hydroxyl bending modes (centered at ∼260 meV). In addition, the poorly defined signals at ∼378 meV (Fig. S3a) are the O–H stretching modes. In the experimental IR or Raman spectra,[19–24] the broad continuum of states related to the O–H stretching modes in diaspore is ascribed to: (i) strong anharmonic mode–mode coupling due to medium-strength HBs; and (ii) coupling with the hydroxyl bending overtones.

3.3 Boehmite

The arrangement of oxygens in boehmite (γ-AlO(OH)) follows a cubic-close-packing sequence, which defines the double sheets of edge-sharing AlO_6 in the *xz* plane (Fig. S2b).[15] Two inequivalent O atoms are present: one is tetrahedrally coordinated by four Al atoms (as a μ_4-O atom) and does not involve any HBs; the other is coordinated by two Al atoms and one H atom, forming a terminal μ_2-OH group on the octahedral double sheets (Fig. S2b). These octahedral double sheets with μ_2-OH groups on each side form a layer structure, which is held together along the *y* direction by interlayer HB cross-linkages (Fig. 3(a)). The μ_2-OH groups are thus both HB donors and acceptors, and create a chain-like pattern (···O–H···O–H···O–H···) in the *yz* plane of the crystal (Fig. 3(a)). Diffraction[44,48–51] and theoretical[25,43,52–54] studies have shown that various H orientation chains can be present along the HB chain (see the SI for more discussion). These affect the energy of the equilibrium structure and generate its instability relative to its polymorph, diaspore.[55]

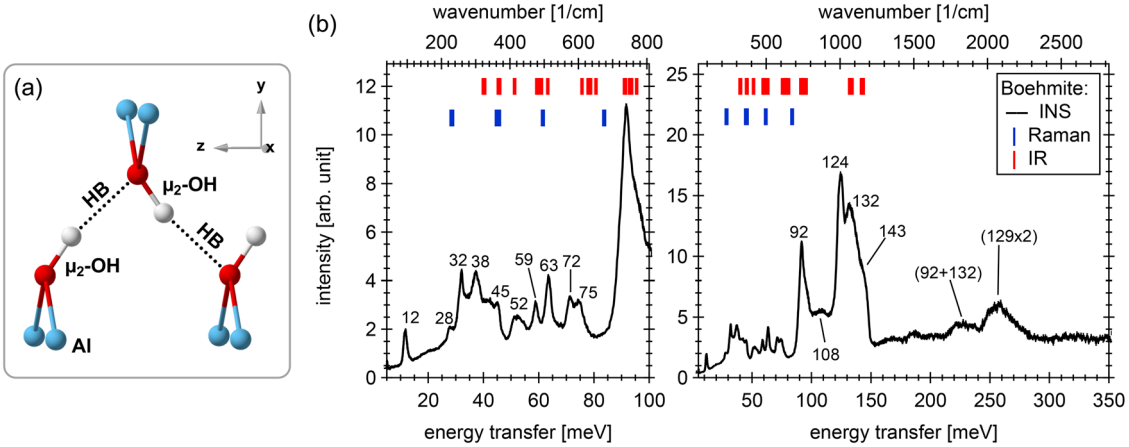

Fig. 3 (a) Local hydrogen bond (HB) cross-linkages in between boehmite's layers. Al, O and H atoms are represented in blue, red and white spheres, respectively. Only the μ_2-OH group is shown; see Fig. S2b for a complete boehmite structure.[15] (b) INS spectrum of boehmite (same spectrum as shown in our recent work[58]) and its comparison to the experimental Raman and IR data from the literature.[19–22,25–27] For simplicity, tick marks are used to label transitions observed by optical spectroscopy. The number labels indicate the energy transfers of the most relevant features in meV. The 12 meV peak is an artifact of the VISION spectrometer.

At the local scale, when a HB is established (Table 1), the unique nature of the Al–O–H bending modes can be observed directly by INS in the librational region (Fig. 3(b)). As shown in Fig. 3(b), the Al–O–H bending modes are spread over a large range from 90 to 155 meV, and several well resolved bands are present at 92, 124, 132 and 143 meV. The intensity of these bands contrast with those in the IR or Raman spectra at similar energies, where hydroxyl bending modes are either forbidden or only show weak/broad intensities (especially in Raman).[19–22,25–27] By comparison, the most intense features of the IR and Raman spectra are in the lower energy range of 20–90 meV (Fig. 3(b)), which corresponds to the various lattice octahedron modes, *e.g.*, AlO_6 shearing deformation (the low energy portion of 20–90 meV) and Al–O stretching modes (the high energy portion of 20–90 meV).[25] The 20–90 meV region of the INS spectrum reveals the relative layer motions caused by interlayer HB interactions, reflecting hydroxyl riding/translational modes, and is generally consistent with the reported IR and Raman bands (Fig. 3(b)). Note that both IR and Raman spectra of boehmite are characterized by a few very strong absorption bands at 20–90 meV, which are typically used for phase identification, while the corresponding INS spectrum is more complex (see Fig. S4 for a direct comparison with the theoretical spectrum).

According to factor group analysis,[25,28] both the strong INS peaks observed at 92 and 143 meV correspond to the in-plane Al–O–H bending mode (movement in the *yz* plane), but the mode is split into in-phase (92 meV) and out-of-phase (143 meV) combinations. The higher transition energy for the out-of-phase mode is caused by the nearby H atoms (along the HB chain) moving in antiphase fashion so that the H···H distance at one extreme of the motion is much shorter than at equilibrium. A similar logic can be used to explain the split of the out-of-plane Al–O–H bending mode (movement normal to the *yz* plane) into out-of-phase (124 meV) and in-phase (132 meV) combinations, depending on whether or not the motion brings H atoms from adjacent units (in the *x* direction) close to each other. As noted by Noel *et al.*,[25] the effects of splitting on the out-of-plane bending mode are much smaller than those on the in-plane bending mode. The 92 meV mode is related to the minimum energy configurations for proton hopping, *i.e.*, hopping as in-phase/in-plane travelling waves along the HB chain. Proton mobility and hopping mechanisms in boehmite are beyond the scope of this work and are discussed in detail by Pan *et al.*[56] and Jiang *et al.*[57]

The weak/broad peak centered around 108 meV (Fig. 3(b)) does not exist in factor group analysis,[25,28] as it is far from any calculated transition energies at the zone center and from peaks arising from critical points elsewhere in the Brillouin zone. This peak likely corresponds to overtones or can be attributed to bending librations of surface hydroxyl groups (*i.e.*, the μ_2-OH groups located at the boehmite surface). Surface hydroxyl species are present in the as-synthesized boehmite, and they can interact with surface-adsorbed water molecules.[26,27] The presence of surface hydroxyl + water species can also be identified in the O–H stretching region using IR or Raman, because they give rise to extra broad bands in addition to the bulk structural O–H stretches centered at about 382 and 406 meV.[27] In general, the separation of four major structural Al–O–H bending modes and the potential presence of surface hydroxyl deformation modes determine the width/shape of the Al–O–H bending bands in the range of 90–155 meV (Fig. 3(b)).

Other features in the INS spectrum, such as a series of weak and broad bands between 170 and 350 meV, correspond to overtone processes. For example, the two broad bands centered at 224 and 258 meV (Fig. 3(b)) are assigned to the combinations of the hydroxyl bending modes (where 129 meV is the center of mass of the two out-of-plane bending modes). The weak intensities at about 200 meV could be associated with the intramolecular H–O–H bending of surface-adsorbed water molecules. Many IR spectra of natural or synthetic boehmites do show H–O–H bending signatures,[21,22,25–27] together with a broadening of the O–H stretching region in the range of 370–420 meV (Fig. S3b).

3.4 Gibbsite and bayerite

Gibbsite (α-$Al(OH)_3$) and bayerite (β-$Al(OH)_3$) share the same layered building block consisting of edge-sharing $Al(OH)_6$ octahedra forming an $Al(OH)_3$ dioctahedral layer.[16,17] The dioctahedral layers lie in the *xy* plane and are stacked along the *z* axis in the sequence of ABBA (in gibbsite; Fig. S2c) or ABAB (in bayerite; Fig. S2d), where A and B stand for the hexagonally packed hydroxyl groups positioned differently on each side of the layer. There are six non-equivalent hydroxyl groups in their structures (Fig. 4(a) and (b)). Each is coordinated to two Al atoms (as a μ_2-OH group) and is involved in HBs in two distinct ways: the interlayer and intralayer HBs (Fig. 4(a), (b) and Table 1). The interlayer hydroxyl groups (OH1, OH2, OH3) are oriented along the *z* axis (Fig. 4(a) and (b)), and are responsible for HB cross-linkages between adjacent layers. The intralayer hydroxyl groups (OH4, OH5, OH6) lie approximatively in the *xy* plane, and point towards cavities in the dioctahedral layer (Fig. 4(a) and (b)). The HB geometries of these six hydroxyl groups are listed in Table 1. Thus, gibbsite and bayerite differ from each other by the intralayer HB orientations and the interlayer shift vectors which, together, lead to variations in the HB strength and geometry. O atoms (O4, O5, O6) of the intralayer hydroxyl groups are acceptors of the interlayer HBs and *vice versa*. The intralayer hydroxyls participate in weaker HBs than the interlayer hydroxyls (Table 1) and, thus, the O–H stretching associated with the intralayer hydroxyls is at higher energies, whereas the interlayer hydroxyl groups generate the lower energy portion of the stretching bands.[16,30]

The similarity of the HB environments in these two polymorphs leads to similar INS spectra in the librational region (Fig. 4(c) and (d)), with the spectrum for bayerite shifted towards lower energy due to an overall weaker HB network. The presence of multiple HB environments and their coupled motions, however, results in complicated hydroxyl librational bands (Fig. 4(c) and (d)). Based on the intensity variations shown in Fig. 4, both spectra can be roughly divided into two main regions: the hydroxyl bending region (82–145 meV), and the hydroxyl riding/translational region (15–82 meV; caused by AlO_6 octahedra modes). There is no gap between these regions and, in the

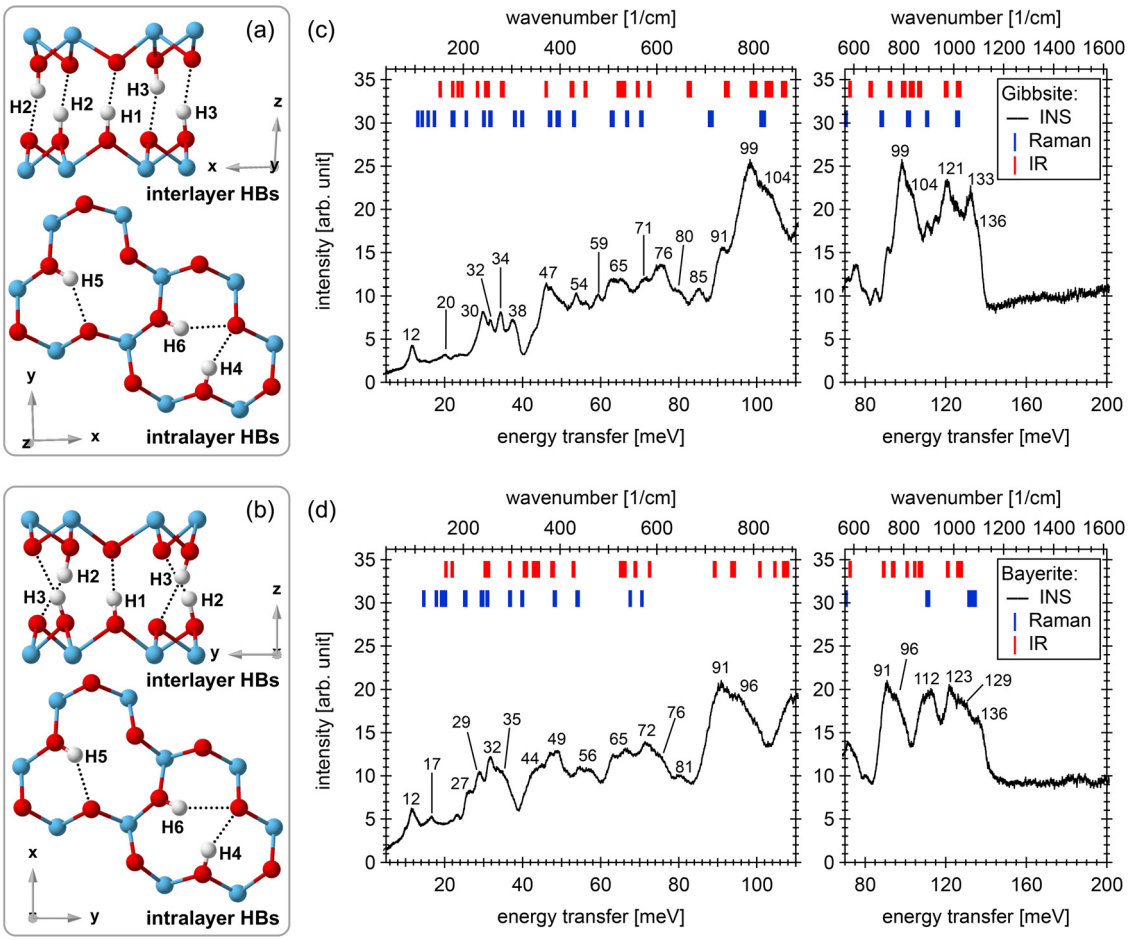

Fig. 4 Local hydrogen bond (dotted lines) environments in gibbsite (a) and bayerite (b). Al, O and H atoms are represented in blue, red and white spheres, respectively. In both structures, hydroxyl groups are all in the μ_2-OH coordination; see Fig. S2c and d for complete structural illustration.[16,17] The INS spectra of gibbsite (c) and bayerite (d), and comparison to experimental Raman and IR data from the literature.[16,19–22,28–30] For simplicity, tick marks are used to label transitions observed by optical spectroscopy (details are described in the text). The number labels indicate the energy transfers of the most relevant features in meV. See Fig. S3c and d for the higher energy transfer region. The 12 meV peak is an artifact of the VISION spectrometer.

overlapping region (about 82–100 meV), modes likely involve both Al–O–H bending and Al–O stretching motions. These observed features are in agreement with the experimental IR and Raman data,[16,19–22,28–30] as well as with theoretical calculations (Fig. S4).

In the hydroxyl bending region (82–145 meV), the Raman spectrum for gibbsite[20,28,29] is characterized by four broad/weak bands at about 88, 101, 111 and 126 meV, and the IR spectrum[21,22,28,29] shows two well-defined bands at 120 and 126 meV, with a broad shoulder at 90–107 meV (Fig. 4(c)). The Raman spectrum for bayerite[20,28] shows two broad bands centered at 112 and 132 meV, and the IR spectrum[21,28] also shows two very broad bands at 121–128 meV and 89–110 meV (Fig. 4(d)). Thus, reliable identification and consistent interpretation of the Al–O–H bending motions in gibbsite and bayerite is challenging. The low structural symmetry in gibbsite and bayerite also makes normal mode analysis difficult, and the INS spectra reflect highly mixed vibrational modes that involve all the atoms in the basic structural units. In addition, the large number of degrees of freedom leads to vibrations of different character overlapping in energy so that a given energy transfer in INS cannot be associated with a unique vibrational motion. Nonetheless, comparison with the calculated VDOS and the associated dynamical matrix eigenvectors allows mode assignments for the most relevant features observed by INS.

For gibbsite (Fig. 4(c)), the highest-energy bands at 136 and 133 meV are from excitations of H2 and H1 atoms, respectively, vibrating tangentially to the hexameric ring of the Al octahedra. These interlayer hydroxyls participate in the shortest HBs in the gibbsite structure (Table 1). The peak at 121 meV mainly reflects the movements of H1, H3 and H4, and the features at 99 and 104 meV are contributed by a combination of H5 and H6. Thus, the locations of the main spectral contributions of these high-energy hydroxyl bending modes show a consistent dependence on the distance (strength) of HBs involved (Table 1). The shoulder at 91 meV is formed by the synchronous motions of interlayer hydroxyl hydrogen H1 and intralayer hydroxyl hydrogen H4, which form a HB donor–acceptor pair and rock in such a way that the ($\measuredangle$H1$\cdots$O4–H4) angle changes little. The broad, complex band between 47 and 85 meV is the

riding mode associated with internal distortions of the AlO_6 octahedra. The stiffest end of this band (above 70 meV) is mainly generated by coupling of intralayer hydroxyl bending (OH4, OH5, OH6) to Al–O stretches.

The nature of the modes at lower-transition energies has also been revealed by other theoretical approaches involving: (i) D isotopic substitution; and (ii) infinite AlO_6 mass substitution.[28] When H atoms are replaced by D, computed normal modes involving D(H) are shifted to the lower energy transfer region. With the infinite AlO_6 mass substitution method, modes to which Al and O contribute significantly shift to much lower energies, while nearly pure H modes only shift moderately. Using this approach, theoretical analyses[28] of the vibrational contributions suggest that: (i) modes in the 40–80 meV region mainly correspond to the stretching of Al–O octahedral bonds (where O atoms show the largest participation); and (ii) below about 40 meV, Al atoms show the largest contributions corresponding to bending/rotational deformation of AlO_6 subunits, and shifting or separation of the layers with respect to each other. This is consistent with our theoretical calculations, in which modes in the 30–40 meV region involve riding of protons on the collective motions of octahedral sheets with neighboring octahedra rocking relative to one another. Below 30 meV, the modes correspond to whole-sheet collective motions.

3.5 Hydroxyl intercalated lithium–aluminum-layered double hydroxide (OH-LiAl-LDH)

In OH-LiAl-LDH, Li^+ occupies the vacant sites of the $Al(OH)_3$ dioctahedral layer. Thus, the layer's μ_2-OH groups favor outward-pointing orientations approximately along the z axis. Such μ_2-OH groups could then establish HBs with intercalated OH^- and H_2O species. The structural positions of these intercalated OH^-/H_2O species are, however, not fully determined. They are likely disordered, yielding a multiplicity of HB configurations. This configurational disorder would account for the breadth of the librational band (Fig. 5).

The principal feature of the OH-LiAl-LDH INS spectrum is the presence of a low-energy librational band edge (LE) at around 45 meV (Fig. 5). Below 45 meV, the translational region consists of four broad peaks (Fig. 5). Between 45 meV and 150 meV, the librational band displays two components: (i) a very broad intensity component similar to that in vitrified aqueous solutions or amorphous systems due to the temporally and spatially disordered HBs; and (ii) four broad peaks at around 72, 92, 101 and 126 meV (Fig. 5), which may be due to the Al–O–H bending or to bending of intercalated OH^-/H_2O species. INS investigations on a related material, chlorine intercalated LiAl-LDH ($Li[Al(OH)_3]_2{\cdot}Cl{\cdot}4H_2O$), showed a similar librational edge and bandwidth from 45 to 150 meV.[60] Attempts to assign the observed broad librational bands using ordered interlayer Cl^-/H_2O arrangements suggested that water molecular librations (rotational oscillations) dominate in the lower energy transfer region (roughly 50–100 meV), whereas O–H bending deformations (in either water molecules or the μ_2-OH groups) dominate at higher energies.[60] Presumably, a similar mode assignment can be applied for OH-LiAl-LDH. The noticeable hump at about 200 meV is from the intramolecular H–O–H bending of the intercalated water molecules with librational band overtones underneath.

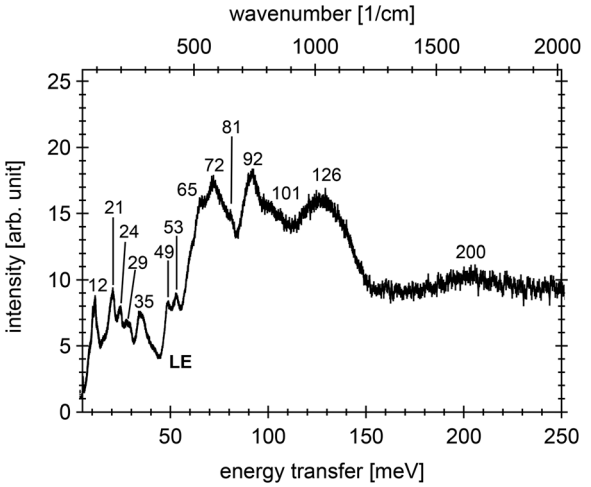

Fig. 5 INS spectrum of the OH-LiAl-LDH sample. The number labels indicate the energy transfers of the most relevant features in meV. LE = librational edge (details in the text). See Fig. S3e, for the higher energy transfer region. The 12 meV peak is an artifact of the VISION spectrometer.

3.6 Bending librations of hydroxyl groups in structurally or chemically analogous materials

Analysis of the published INS spectra of analogous materials can be used to establish correlations between hydroxyl bending energies and the strength and geometry of HB interactions. Fig. 6 shows the observed hydroxyl bending peaks plotted against the mean HB distance of each material structure. For example, in diaspore, the two hydroxyl bending peaks centered at 126 and 145 meV (Fig. 2(b)) are correlated to a HB distance of 1.692 Å (Table 1). In boehmite, the four hydroxyl bending peaks at 92, 124, 132 and 143 meV (Fig. 3(b)) are correlated to a HB distance of 1.814 Å (Table 1). In gibbsite and bayerite, the relevant hydroxyl bending peaks (labelled in Fig. 4(c) and (d)) are related to the mean HB distance of 2.013 Å in gibbsite and 2.129 Å in bayerite (Table 1; average of all 6 HBs in each mineral case). We performed the same analysis on goethite α-FeO(OH)[61–63] (isostructural to diaspore), lepidocrocite γ-FeO(OH)[15,61,64] (isostructural to boehmite), kaolinite[65,66] (has a dioctahedral alumina layer as in gibbsite/bayerite), and three alkaline aluminate salts[67] ($K_2[Al_2O(OH)_6]$, $Rb_2[Al_2O(OH)_6]$, and $Cs[Al(OH)_4]{\cdot}2H_2O$). Fig. 6 (right-hand side) shows the structural hydroxyl groups participating in HB with the neighboring O atom (in accordance with the HB geometric definition[47]). Despite band dispersion, splitting, and coupling effects, which produce complicated band shapes, the majority of the upper librational band edges for these materials fall on a straight line (bold-black solid line in Fig. 6) and display the expected blueshift to higher energy with decreasing HB distances (*i.e.*, increasing HB strengths). The mean HB distance in OH-LiAl-LDH is unknown (because of the undetermined structure), and thus, the distance (~2.2 Å; Fig. 6) was estimated from a linear correlation based on its highest-energy bending peak position at ~126 meV (Fig. 5).

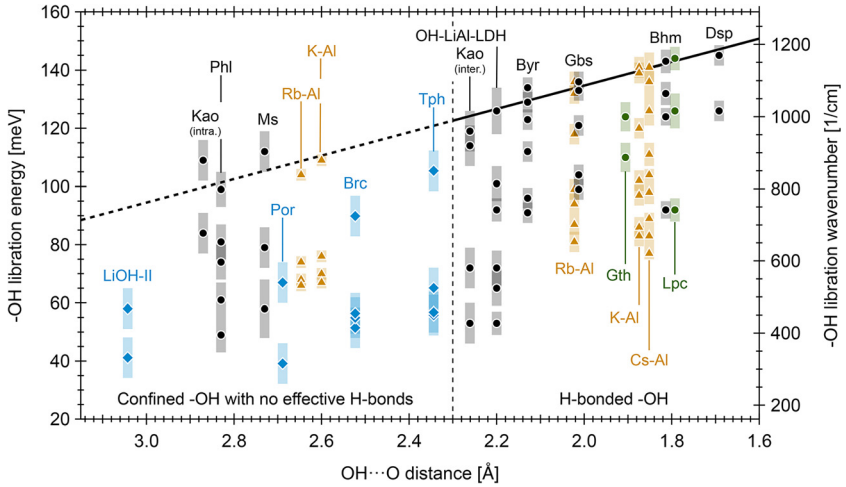

Fig. 6 Relation between hydroxyl bending modes and the mean (O–H···O) HB distance for the selected analogous materials, showing upshifting (blueshift) in the upper librational band edge with respect to the mean HB distances. The bold-black solid line and its extension (dashed line) to the long HB distances highlight the observed linear correlation. The circle, triangle, and diamond symbols mark the peak center position (in meV or cm^{-1}), and the shaded bars describe the ± peak width at half maximum. Symbol colors are used for clarity only, and do not tie to specific material cases. Mineral abbreviations are: diaspore (Dsp), boehmite (Bhm), gibbsite (Gbs), bayerite (Byr), lepidocrocite (Lpc), goethite (Gth), kaolinite (Kao), muscovite (Ms), phlogopite (Phl), theophrastite (Tph), brucite (Brc), and portlandite (Por). Other abbreviations are: OH-LiAl-LDH for hydroxyl intercalated lithium-aluminum-layered double hydroxide, K-Al for $K_2[Al_2O(OH)_6]$ (K-Al), Rb-Al for $Rb_2[Al_2O(OH)_6]$, and Cs-Al for $Cs[Al(OH)_4]\cdot 2H_2O$.

A clear linear correlation was not, however, observed for structural hydroxyl groups with no appreciable HB formation (Fig. 6; left-hand side with HB distances >2.3 Å), in which multiple neighboring O atoms around each hydroxyl group (*i.e.*, multi-furcated interactions) eliminate the close approach and geometry needed for HB formation. A typical example of such steric hindrance is the confined intralayer hydroxyl group in kaolinite's 1 : 1 layer, where the O–H vector is oriented toward the vacant site in the octahedral net and is not involved in any effective HB formation (Fig. 6; the mean HB distance is about 2.871 Å[66]). Muscovite and phlogopite possess similar intralayer hydroxyl groups that form no effective HBs within their 2 : 1 layer units (Fig. 6; black circles on the left-hand side).[68–72] Similarly, two out of the six aluminate–OH ligands in potassium and rubidium aluminate salts ($K_2[Al_2O(OH)_6]$ and $Rb_2[Al_2O(OH)_6]$) do not participate in HB interactions, and their corresponding Al–O–H bending modes are located at lower energies (Fig. 6; brown triangles on the left-hand side),[67] reflecting the weakening of the restoring forces. In addition, some layered metal hydroxides (*e.g.*, theophrastite–$Ni(OH)_2$,[10] brucite–$Mg(OH)_2$,[10,73,74] portlandite–$Ca(OH)_2$,[73,75] and LiOH-II[73,76,77]) have their hydroxyl groups pointing towards the interlayer space but do not form effective HBs crossing the interlayer. Four of these, plotted in Fig. 6 (blue diamonds on the left-hand side), show a further deviation from the linear correlation extending from the short HB distance region. In general, hydroxyl bending librations occur at lower-energy for structural hydroxyl groups with no appreciable HB interactions, and couple easily with metal–oxygen (M–O) lattice modes, making them less suitable for correlation studies. Their exact libration energies likely depend on the covalency of the M–O bonds and on the external electric fields exerted on the hydroxyl groups.

3.7 Correlation between O–H stretching and upper librational band edge energy

Where protons participate in HBs, we can relate the position of the upper librational band edge to the O–H stretching energy (frequency) and HB strength,[78,79] as the energy of the O–H stretching of a given covalent O–H bond is anticorrelated with the energy of the bending libration of the same bond. The VDOS from our phonon calculations projected onto each crystallographically distinct H site (Fig. 7; using diaspore, boehmite, gibbsite and bayerite as examples) demonstrates this relationship. In Fig. 7, each line is colored according to the (O–H···O) HB distance (blue for the shortest and red for the longest). The qualitative trends are explained by a simple picture in which the vibrational motion of an H atom is determined by its HB environment. In the stretching region, long HB distances (red curves) in gibbsite and bayerite have the stiffest stretching vibrations and the most electron density residing in the covalent O–H bond being stretched. The short HB distances (blue curves for diaspore and boehmite) have lower stretching energies. As all the O–H stretches occur above 350 meV (Fig. 7) there are no other vibrations to mix with, making classification unambiguous. In the direction perpendicular to the (O–H···O) line, the restoring force for H displacement is set by the cost of disturbing the HB by increasing the (∢H–O···O) angle. Stronger HB interactions, therefore, have higher bending energy, and the strongest HB in a material should set the upper librational band edge in the INS spectra. This explains the correlation in Fig. 6. For weaker HB interactions, the restoring force for transverse H displacement is small enough that the bending librations fall in the spectral range of bond stretches involving heavier atoms (*e.g.*, AlO_6 octahedra). In this case hydroxyl bending motions are mixed with

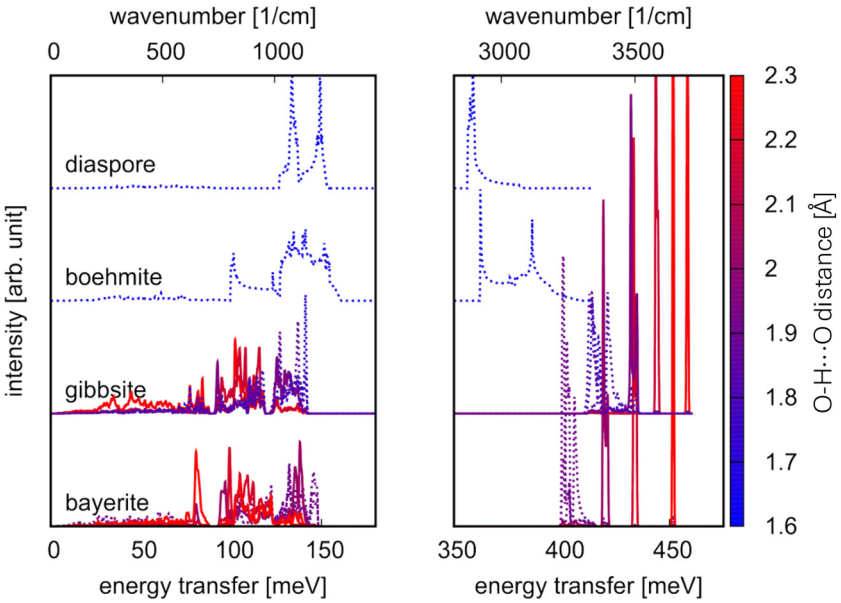

Fig. 7 Relationship between the intramolecular O–H stretching and upper librational band edge energies, showing the H-VDOS calculations for diaspore, boehmite, gibbsite and bayerite examples. Dotted and solid lines represent HBs that do and do not connect separate layers, respectively.

framework deformations, and mode classification becomes ambiguous. For example, the VDOS projected onto an H atom associated with intralayer hydroxyl groups in gibbsite and bayerite is distributed over a large frequency range from the lower librational bands (~90 meV in these materials) down to ~20 meV (Fig. 7).

Correlation between O–H stretching and hydroxyl bending energy was demonstrated by Novak[2] who showed a linear increase of bending energy with decreasing O–H stretching energy for the (O–H···O) interactions in carboxylic acids and their acid salts. In the compound system Novak[2] investigated, the lower-energy out-of-plane bending mode was correlated to the O–H stretching, as the higher-energy in-plane bending mode contains vibrational coupling, making it less suitable for correlation studies. For the materials shown in Fig. 6, the upper librational band edge energy is correlated to the distance (strength) of their HBs, as it is less likely to couple with the low-energy lattice modes. Hence, when either the stretching or bending energy (or a combination of both) is used to estimate HB distance in the corresponding hydroxyl group, vibrational coupling or mixing effects need to be considered.

3.8 Spectroscopic insights into the interlayer HB orientation in boehmite

In the last section, we focused on boehmite's interlayer HB structure for two reasons: (i) it represents a prototypical layered material with (exclusively) interlayer HB cross-linkages, and (ii) unlike gibbsite/bayerite, its hydroxyl bending librations (lowest at 92 meV) do not extend into the Al–O lattice mode region. This separation allows an opportunity to demonstrate the sensitivity of INS for the characterization of HB orientation and the nature of layer stacking. Recall that modes in the 20–90 meV region in boehmite arise from participation of H in the lattice dynamics (known as hydroxyl riding modes). When combined with theory, detailed mode assignments of the array of characteristic peaks can be performed (Fig. 8).

Fig. 8(a) shows two possible symmetries corresponding to protons in the top layer lying in the same (*Pnma*), or opposite ($Cmc2_1$), direction as those on the bottom layer, with respect to the *z* axis. These two choices (both *Cmcm* subgroups) produce HB orientations originally described in the *Cmcm* structure (with partial H occupancies; see the SI for the *Cmcm* space group descriptions) and result in H-projected VDOS patterns compatible with the experimental INS spectrum (Fig. 8(b), peaks numbered for reference). Peak 1 is associated with relative lateral motions of two adjacent AlO(OH) layers in opposite directions. If adjacent layers were stacked in registry instead of offset in a checkerboard pattern, the unit cell would be halved along the *y* axis, and these modes would show a peak (peak 1) corresponding to the critical point at (0, 1/2, 0) in the reciprocal space. In the two-layer unit-cell setting (Fig. 8(a)), they appear as bands folded back to the Γ point. Peaks 2–11 arise from the internal motions of the octahedral sheets. There is a clear correspondence between the calculated H-VDOS and observed INS peaks, with agreement within 2 meV in the peak positions and clear similarities in peak shapes (Fig. 8(b)). The calculated low-energy lattice modes (indirectly probed by INS as hydroxyl riding) contrast with the hydroxyl bending and intramolecular O–H stretching at higher energies, the latter of which have the correct peak shape, but the peak positions are displaced by about 10–30 meV in the simulations. This discrepancy, which is in opposite directions for the bending and stretching modes (*i.e.*, simulations typically underestimate the bending peak position and overestimate the stretching modes[80]), is not reduced by neglecting the dispersion (D3) corrections and is consistent with similar behavior observed in our study of alkali aluminate salts.[67]

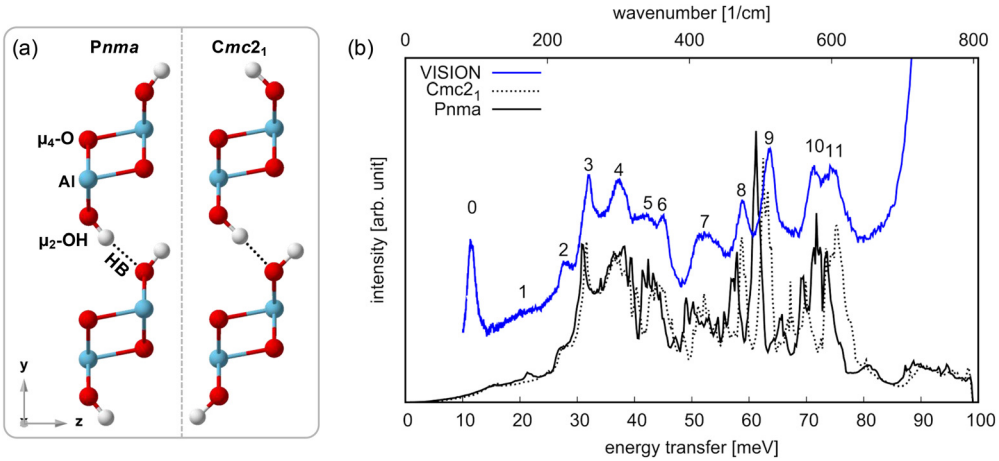

Fig. 8 (a) Two possible HB orientations in the crystal structure of boehmite. The unit cell of both lower symmetry structures (*Cmc*2$_1$ and *Pnma*) follows effectively the original *Cmcm* description. (b) Comparison between the observed INS (blue) and calculated H-projected VDOS patterns using the *Cmc*2$_1$ (dotted black) and *Pnma* (solid black) settings. Peak 0 (at 12 meV) is an artifact of the VISION spectrometer.

We also checked the effects of using a hybrid functional (in this case, PBE0[81]) in smaller boehmite test calculations done with 'loose' parameters. Namely, we set the energy cutoff to 400 eV, reduced the *k*-grid to 2 × 2 × 4, and computed the force constants in the primitive boehmite unit cell. We performed relaxations and lattice dynamics simulations in this more tractable, but numerically unconverged setting using the PBE-D3 approximation and PBE0-D3. Note that PBE-D3 was used for all other calculations in this work. The PBE0-D3 calculations show weaker HBs evident in: (i) a lattice parameter normal to the layers increased by 0.43 Å, (ii) a librational band that is redshifted ∼7 meV, and (iii) O–H stretching bands blueshifted by ∼60 meV, relative to the PBE-D3 calculation done with the same settings. The region below ∼90 meV was nearly identical between the PBE0-D3 and PBE-D3 calculations. Hence, we conclude that PBE0-D3 (or plain PBE0) would likely remove some of the systematic errors observed in the locations of the librational bands in the simulations reported here, but our extrapolations predict that the upper librational band edge would still be overestimated by ∼10 meV. Unfortunately, hybrid calculations using converged supercells and basis sets were not feasible using the methods of this work. This points to the need for a systematic study of the exchange–correlation dependence of simulated INS using DFT.

Peaks 10 and 11 are both strong (Fig. 8(b)). Peak 10 is identified in the simulation with the *Pnma* setting, but peak 11 is absent. The reverse situation holds for the *Cmc*2$_1$ simulation. In both symmetry settings, these two peaks reflect motions in which Al–O–H groups move along the *z* axis in the common plane containing (O–H···O) HB motifs. The different couplings, through the AlO(OH) octahedral layers, and between the orientations of the hydroxyls on opposite sides of the layers are reflected in the different energies. The occurrence of both peaks in the INS spectrum suggests that the synthetic boehmite studied here contained both possible local HB orientations (Fig. 8(a)). Peaks 10 and 11 have nearly the same intensity, indicating that roughly half of the layers have HB chains pointing the same way and half have HB chains in opposite directions. This suggests that the directions of the HB chains are uniformly random from one layer to the next. This finding highlights the value of INS spectroscopy for studying correlated proton disorder.

4. Conclusions

We have presented comprehensive INS data from 20 to 200 meV of diaspore, boehmite, gibbsite, bayerite, and hydroxyl intercalated lithium–aluminum-layered double hydroxide (OH-LiAl-LDH). Key spectral features reflecting the structure and dynamics of protons in these materials have been discussed, highlighting the complementary nature of INS and optical spectroscopic and computational studies. We have shown that the upper librational band edge reflects the strength of HBs by correlating the current measurements and existing literature data with HB geometry. Using DFT simulations, we extended this correlation to the intramolecular O–H stretching region, showing the relationship between the bending librations (probed by INS) and more conventional spectroscopic interrogation of HB strength using IR and Raman. In the lower energy region, the crossover from the onset of hydroxyl bending to mixing with riding/lattice modes is determined by the weakest HB in the material. Finally, we demonstrated that INS can be used to study details of the translational (0–100 meV) region and that peaks in this region can be used, in conjunction with theoretical analysis, to identify correlated proton disorder that cannot be measured by diffraction or optical spectroscopy.

Notice

Author contributions

H.-W. W., M. P. P., T. L., L. D., A. I. K., and L. M. A. made contributions to the experimental design, data acquisition and analysis. T. R. G. and X. Z. synthesized and characterized materials for this work. G. K. S., K. M. R., C. I. P., and all authors discussed the results and edited the manuscript. L. M. A. and C. I. P. also supervised the work. The manuscript was prepared by H.-W. W. and M. P. P. with input from all authors.

Conflicts of interest

The authors declare no competing interests.

Data availability

The data supporting this article have been included as part of the supplementary information (SI). Supplementary information includes supporting texts and Fig. S1–S4. See DOI: https://doi.org/10.1039/d5cp03788c.

Acknowledgements

This work was supported by Ion Dynamics in Radioactive Environments and Materials (IDREAM; FWP 68932), an Energy Frontier Research Center funded by the U.S. Department of Energy (DOE), Office of Science, Basic Energy Sciences (BES). Neutron science experiments were designed at Oak Ridge National Laboratory (ERKCG08). A portion of this research used resources at the Spallation Neutron Source, a DOE Office of Science User Facility operated by the Oak Ridge National Laboratory. We would like to thank Rudi Wobito (Wobito Gems) and Jilienne Hart Arth (Erica Courtney Inc.) for the gem diaspore used in this study.

References

1 A. W. Naumann, G. J. Safford and F. A. Mumpton, Low-Frequency (OH)-Motions in Layer Silicate Minerals, *Clays and Clay Minerals*, Pergamon, 1966, pp. 367–383.
2 A. Novak, Hydrogen Bonding in Solids. Correlation of Spectroscopic and Crystallographic Data, *Large Molecules. Structure and Bonding, 18*, Springer, Berlin, Heidelberg, 1974.
3 H. D. Lutz, W. Eckers and H. Haeuseler, OH Stretching Frequencies of Solid Hydroxides and of Free OH^- Ions, *J. Mol. Struct.*, 1982, **80**, 221–224.
4 J. Tomkinson, The Vibrations of Hydrogen Bonds, *Spectrochim. Acta, Part A*, 1992, **48**, 329–348.
5 K. Beckenkamp and H. D. Lutz, Lattice Vibration Spectra Part LXXII. OH Stretching Frequencies of Solid Hydroxides—Correlation with Structural and Bonding Data, *J. Mol. Struct.*, 1992, **270**, 393–405.
6 H. D. Lutz, Hydroxide Ions in Condensed Materials—Correlation of Spectroscopic and Structural data, *Coordination Chemistry*, Springer, Berlin, Heidelberg, 1995, pp. 85–103.
7 C. M. B. Line and G. J. Kearley, An Inelastic Incoherent Neutron Scattering Study of Water in Small-Pored Zeolites and Other Water-Bearing Minerals, *J. Chem. Phys.*, 2000, **112**, 9058–9067.
8 D. Xu, S. Zhang, H. Tong, L. Wang and N. Xu, Low-Frequency Vibrational Density of States of Ordinary and Ultra-Stable Glasses, *Nat. Commun.*, 2024, **15**, 1424.
9 F. Shi, H.-L. Dong, D. Zhou, C.-H. Wang, Q.-L. Tan, J.-J. Xiong and Q. Wang, Lattice Dynamics and Phonon Characteristics of Complex Perovskite Microwave Ceramics, *IET Nanodielectr.*, 2019, **2**, 11–26.
10 V. Y. Kazimirov, M. B. Smirnov, L. Bourgeois, L. Guerlou-Demourgues, L. Servant, A. M. Balagurov, I. Natkaniec, N. R. Khasanova and E. V. Antipov, Atomic Structure and Lattice Dynamics of Ni and Mg Hydroxides, *Solid State Ionics*, 2010, **181**, 1764–1770.
11 H. W. Wang, M. J. DelloStritto, N. Kumar, A. I. Kolesnikov, P. R. C. Kent, J. D. Kubicki, D. J. Wesolowski and J. O. Sofo, Vibrational Density of States of Strongly H-Bonded Interfacial Water: Insights from Inelastic Neutron Scattering and Theory, *J. Phys. Chem. C*, 2014, **118**, 10805–10813.
12 B. Civalleri, P. Ugliengo, C. M. Zicovich-Wilson and R. Dovesi, Ab Initio Modeling of Layered Materials With the CRYSTAL Code: An Overview, *Z. Kristallogr.*, 2009, **224**, 241–250.
13 S. F. Parker, K. Refson, R. I. Bewley and G. Dent, Assignment of The Vibrational Spectra of Lithium Hydroxide Monohydrate, $LiOH{\cdot}H_2O$, *J. Chem. Phys.*, 2011, **134**, 084503.
14 R. J. Hill, Crystal Structure Refinement and Electron Density Distribution in Diaspore, *Phys. Chem. Miner.*, 1979, **5**, 179–200.
15 A. N. Christensen, M. S. Lehmann and P. Convert, Deuteration of Crystalline Hydroxides. Hydrogen Bonds of γ-AlOOH(H,D) and γ-FeOOH(H,D), *Acta Chem. Scand. A*, 1982, **36**, 303–308.
16 E. Balan, M. Lazzeri, G. Morin and F. Mauri, First-Principles Study of the OH-Stretching Modes of Gibbsite, *Am. Mineral.*, 2006, **91**, 115–119.
17 F. Zigan, W. Joswig and N. Burger, Die Wasserstoffpositionen im Bayerit, $Al(OH)_3$, *Z. Kristallogr. Cryst. Mater.*, 1978, **148**, 255–274.
18 T. R. Graham, J. Z. Hu, X. Zhang, M. Dembowski, N. R. Jaegers, C. Wan, M. Bowden, A. S. Lipton, A. R. Felmy, S. B. Clark, K. M. Rosso and C. I. Pearce, Unraveling Gibbsite Transformation Pathways into LiAl-LDH in Concentrated Lithium Hydroxide, *Inorg. Chem.*, 2019, **58**, 12385–12394.
19 H. D. Ruan, R. L. Frost and J. T. Kloprogge, Application of Near-Infrared Spectroscopy to the Study of Alumina Phases, *Appl. Spectrosc.*, 2001, **55**, 190–196.

20 H. D. Ruan, R. L. Frost and J. T. Kloprogge, Comparison of Raman Spectra in Characterizing Gibbsite, Bayerite, Diaspore and Boehmite, *J. Raman Spectrosc.*, 2001, **32**, 745–750.
21 H. D. Ruan, R. L. Frost, J. T. Kloprogge and L. Duong, Far-Infrared Spectroscopy of Alumina Phases, *Spectrochim. Acta, Part A*, 2002, **58**, 265–272.
22 J. T. Kloprogge, H. D. Ruan and R. L. Frost, Thermal Decomposition of Bauxite Minerals: Infrared Emission Spectroscopy of Gibbsite, Boehmite and Diaspore, *J. Mater. Sci.*, 2002, **37**, 1121–1129.
23 R. Demichelis, Y. Noel, B. Civalleri, C. Roetti, M. Ferrero and R. Dovesi, The Vibrational Spectrum of α-AlOOH Diaspore: An *Ab Initio* Study with the CRYSTAL Code, *J. Phys. Chem. B*, 2007, **111**, 9337–9346.
24 S. Delattre, E. Balan, M. Lazzeri, M. Blanchard, M. Guillaumet, O. Beyssac, E. Haussühl, B. Winkler, E. K. H. Salje and G. Calas, Experimental and Theoretical Study of the Vibrational Properties of Diaspore (α-AlOOH), *Phys. Chem. Miner.*, 2012, **39**, 93–102.
25 Y. Noel, R. Demichelis, F. Pascale, P. Ugliengo, R. Orlando and R. Dovesi, *Ab Initio* Quantum Mechanical Study of γ-AlOOH Boehmite: Structure and Vibrational Spectrum, *Phys. Chem. Miner.*, 2009, **36**, 47–59.
26 T. Sun, Q. Zhuo, Y. Chen and Z. Wu, Synthesis of Boehmite and its Effect on Flame Retardancy of Epoxy Resin, *High Perform. Polym.*, 2014, **27**, 100–104.
27 S.-L. Wang, C. T. Johnston, D. L. Bish, J. L. White and S. L. Hem, Water-Vapor Adsorption and Surface Area Measurement of Poorly Crystalline Boehmite, *J. Colloid Interface Sci.*, 2003, **260**, 26–35.
28 R. Demichelis, Y. Noël, P. Ugliengo, C. M. Zicovich-Wilson and R. Dovesi, Physico-Chemical Features of Aluminum Hydroxides As Modeled with the Hybrid B3LYP Functional and Localized Basis Functions, *J. Phys. Chem. C*, 2011, **115**, 13107–13134.
29 R. L. Frost, J. T. Kloprogge, S. C. Russell and J. L. Szetu, Vibrational Spectroscopy and Dehydroxylation of Aluminum (Oxo)hydroxides: Gibbsite, *Appl. Spectrosc.*, 1999, **53**, 423–434.
30 E. Balan, M. Blanchard, J.-F. Hochepied and M. Lazzeri, Surface Modes in the Infrared Spectrum of Hydrous Minerals: The OH Stretching Modes of Bayerite, *Phys. Chem. Miner.*, 2008, **35**, 279–285.
31 M. Hatipoglu and S. C. Chamberlain, A Gem Diaspore Occurrence near Pinarcik, Mugla, Turkey, *Rocks Miner.*, 2011, **86**, 242–249.
32 X. Zhang, W. Cui, K. L. Page, C. I. Pearce, M. E. Bowden, T. R. Graham, Z. Shen, P. Li, Z. Wang, S. Kerisit, A. T. N'Diaye, S. B. Clark and K. M. Rosso, Size and Morphology Controlled Synthesis of Boehmite Nanoplates and Crystal Growth Mechanisms, *Cryst. Growth Des.*, 2018, **18**, 3596–3606.
33 X. Zhang, X. Zhang, T. R. Graham, C. I. Pearce, B. L. Mehdi, A. T. N'Diaye, S. Kerisit, N. D. Browning, S. B. Clark and K. M. Rosso, Fast Synthesis of Gibbsite Nanoplates and Process Optimization using Box-Behnken Experimental Design, *Cryst. Growth Des.*, 2017, **17**, 6801–6808.
34 P. A. Seeger, L. L. Daemen and J. Z. Larese, Resolution of VISION, A Crystal-Analyzer Spectrometer, *Nucl. Instrum. Methods Phys. Res., Sect. A*, 2009, **604**, 719–728.
35 Y. Q. Cheng, L. L. Daemen, A. I. Kolesnikov and A. J. Ramirez-Cuesta, Simulation of Inelastic Neutron Scattering Spectra Using OCLIMAX, *J. Chem. Theory Comput.*, 2019, **15**, 1974–1982.
36 O. Arnold, J. C. Bilheux, J. M. Borreguero, A. Buts, S. I. Campbell, L. Chapon, M. Doucet, N. Draper, R. Ferraz Leal, M. A. Gigg, V. E. Lynch, A. Markvardsen, D. J. Mikkelson, R. L. Mikkelson, R. Miller, K. Palmen, P. Parker, G. Passos, T. G. Perring, P. F. Peterson, S. Ren, M. A. Reuter, A. T. Savici, J. W. Taylor, R. J. Taylor, R. Tolchenov, W. Zhou and J. Zikovsky, Mantid—Data Analysis and Visualization Package for Neutron Scattering and μ SR experiments, *Nucl. Instrum. Methods Phys. Res., Sect. A*, 2014, **764**, 156–166.
37 G. Kresse and J. Furthmuller, Efficient Iterative Schemes for *Ab Initio* Total-Energy Calculations Using a Plane-Wave Basis Set, *Phys. Rev. B: Condens. Matter Mater. Phys.*, 1996, **54**, 11169–11186.
38 A. Togo, First-principles Phonon Calculations with Phonopy and Phono3py, *J. Phys. Soc. Jpn.*, 2023, **92**, 012001.
39 J. P. Perdew, K. Burke and M. Ernzerhof, Generalized Gradient Approximation Made Simple, *Phys. Rev. Lett.*, 1996, **77**, 3865–3868.
40 S. Grimme, Semiempirical GGA-type Density Dunctional Constructed with a Long-range Dispersion Correction, *J. Comput. Chem.*, 2006, **27**, 1787–1799.
41 S. Grimme, J. Antony, S. Ehrlich and H. Krieg, A Consistent and Accurate *Ab Initio* Parametrization of Density Functional Dispersion Correction (DFT-D) for the 94 Elements H-Pu, *J. Chem. Phys.*, 2010, **132**, 154104.
42 P. E. Blöchl, Projector Augmented-Wave Method, *Phys. Rev. B: Condens. Matter Mater. Phys.*, 1994, **50**, 17953–17979.
43 M. Digne, P. Sautet, P. Raybaud, P. Euzen and H. Toulhoat, Hydroxyl Groups on γ-Alumina Surfaces: A DFT Study, *J. Catal.*, 2002, **211**, 1–5.
44 X. Bokhimi, J. A. Toledo-Antonio, M. L. Guzmán-Castillo and F. Hernández-Beltrán, Relationship between Crystallite Size and Bond Lengths in Boehmite, *J. Solid State Chem.*, 2001, **159**, 32–40.
45 D. A. Ksenofontov and Y. K. Kabalov, Structure Refinement and Thermal Stability of Gibbsite, *Inorg. Mater.*, 2012, **48**, 142–144.
46 R. Rothbauer, F. Zigan and H. O'Daniel, Verfeinerung der Struktur des Bayerits, $Al(OH)_3$, *Z. Kristallogr. Cryst. Mater.*, 1967, **125**, 317–331.
47 A. Luzar and D. Chandler, Effect of Environment on Hydrogen Bond Dynamics in Liquid Water, *Phys. Rev. Lett.*, 1996, **76**, 928–931.
48 G. G. Christoph, C. E. Corbató, D. A. Hofmann and R. T. Tettenhorst, The Crystal Structure of Boehmite, *Clays Clay Miner.*, 1979, **27**, 81–86.
49 R. J. Hill, Hydrogen Atoms in Boehmite: A Single Crystal X-Ray Diffraction and Molecular Orbital Study, *Clays Clay Miner.*, 1981, **29**, 435–445.
50 C. E. Corbató, R. T. Tettenhorst and G. G. Christoph, Structure Refinement of Deuterated Boehmite, *Clays Clay Miner.*, 1985, **33**, 71–75.

51 X. Bokhimi, J. Sánchez-Valente and F. Pedraza, Crystallization of Sol–Gel Boehmite via Hydrothermal Annealing, *J. Solid State Chem.*, 2002, **166**, 182–190.
52 A. Chroneos, K. Desai, S. E. Redfern, M. O. Zacate and R. W. Grimes, New Atomic Acale Aimulation Models for Hydroxides and Oxyhydroxides, *J. Mater. Sci.*, 2006, **41**, 675–687.
53 K. M. Rosso and J. R. Rustad, Structures and energies of AlOOH and FeOOH polymorphs from plane wave pseudopotential calculations, *Am. Mineral.*, 2001, **86**, 312–317.
54 M. P. Prange, X. Zhang, M. E. Bowden, Z. Shen, E. S. Ilton and S. N. Kerisit, Predicting Surface Energies and Particle Morphologies of Boehmite (γ-AlOOH) from Density Functional Theory, *J. Phys. Chem. C*, 2018, **122**, 10400–10412.
55 S. Casassa and R. Demichelis, Relative Energy of Aluminum Hydroxides: The Role of Electron Correlation, *J. Phys. Chem. C*, 2012, **116**, 13313–13321.
56 X. Pan, W. Yang, Y. Xie, Y. Chen and H. Guo, Energy Barrier of Proton Transfer in 3d Transition Metal-Doped Boehmite, *J. Phys. Chem. C*, 2021, **125**, 3804–3810.
57 Y. Jiang, Y. Xie and H. Guo, A Computational Study of Energy Barriers of Structural Transformations and Hydrogen Transfer in Boehmite, *RSC Adv.*, 2018, **8**, 2377–2384.
58 L. M. Anovitz, G. Schenter, J. Chun, M. P. Prange, H.-W. Wang, T. Liu, Y. Cheng, L. Daemen, W. Smith, X. Zhang, C. I. Pearce, M. G. Tucker, A. I. Kolesnikov, N. Jalarvo, E. Mamontov and A. G. Stack, Unveiling the Structure and Dynamics of Water Confined in Colloidal Boehmite Suspensions, *Langmuir*, 2025, **41**, 20463–20480.
59 G. A. Jeffrey, *An Introduction to Hydrogen Bonding*, Oxford University Press, 1997.
60 L. Wu, S. F. Evans, Y. Cheng, A. Navrotsky, B. A. Moyer, S. Harrison and M. P. Paranthaman, Neutron Spectroscopic and Thermochemical Characterization of Lithium–Aluminum-Layered Double Hydroxide Chloride: Implications for Lithium Recovery, *J. Phys. Chem. C*, 2019, **123**, 20723–20729.
61 P. G. Hall, N. S. Clarke and S. C. P. Maynard, Inelastic Neutron Scattering (TFXA) Study of Hydrogen Modes in α-FeOOH (Goethite) and γ-FeOOH (Lepidocrocite), *J. Phys. Chem.*, 1995, **99**, 5666–5673.
62 H. Yang, R. Lu, R. T. Downs and G. Costin, Goethite, α-FeO(OH), from Single-Crystal Data, *Acta Crystallogr., Sect. E: Struct. Rep. Online*, 2006, **62**, i250–i252.
63 A. F. Gualtieri and P. Venturelli, In Situ Study of the Goethite-Hematite Phase Transformation by Real Time Synchrotron Powder Diffraction, *Am. Mineral.*, 1999, **84**, 895–904.
64 H. Christensen and A. N. Christensen, Hydrogen Bonds of γ-FeOOH, *Acta Chem. Scand., Ser. A*, 1978, **32**, 87–88.
65 Ľ. Smrčok, D. Tunega, A. J. Ramirez-Cuesta and E. Scholtzová, The Combined Inelastic Neutron Scattering and Solid State DFT Study of Hydrogen Atoms Dynamics in a Highly Ordered Kaolinite, *Phys. Chem. Miner.*, 2010, **37**, 571–579.
66 R. B. Neder, M. Burghammer, T. H. Grasl, H. Schulz, A. Bram and S. Fiedler, Refinement of the Kaolinite Structure From Single-Crystal Synchrotron Data, *Clays Clay Miner.*, 1999, **47**, 487–494.
67 M. P. Prange, T. R. Graham, R. Gorniak, M. Pouvreau, M. Dembowski, H.-W. Wang, L. L. Daemen, G. K. Schenter, M. E. Bowden, E. T. Nienhuis, K. M. Rosso, A. E. Clark and C. I. Pearce, Theory-Guided Inelastic Neutron Scattering of Crystalline Alkaline Aluminate Salts Bearing Principal Motifs of Solution-State Species, *Inorg. Chem.*, 2021, **60**, 16223–16232.
68 L. Smrčok, M. Rieder, A. I. Kolesnikov and G. E. Granroth, Combined Inelastic Neutron Scattering and Solid-State Density Functional Theory Study of Dynamics of Hydrogen Atoms in Muscovite 2M1, *Am. Mineral.*, 2011, **96**, 301–307.
69 L. Smrčok, A. I. Kolesnikov and M. Rieder, Combined Inelastic Neutron Scattering and Solid-State DFT Study of Dynamics of Hydrogen Atoms in Trioctahedral 1M Phlogopite, *Phys. Chem. Miner.*, 2012, **39**, 779–787.
70 V. R. Rothbauer, Untersuchung Eines 2M1-Muskovits mit Neutronenstrahlen, *Neues Jahrb. Mineral., Monatsh.*, 1971, **4**, 143–154.
71 M. Catti, G. Ferraris, S. Hull and A. Pavese, Powder Neutron Diffraction Study of 2M1 Muscovite at Room Pressure and at 2 GPa, *Eur. J. Mineral.*, 1994, **6**, 171–178.
72 G. J. Redhammer and G. Roth, Single-Crystal Structure Refinements and Crystal Chemistry of Synthetic Trioctahedral Micas $KM_3(Al^{3+},Si^{4+})_4O_{10}(OH)_2$, where M = Ni^{2+}, Mg^{2+}, Co^{2+}, Fe^{2+}, or Al^{3+}, *Am. Mineral.*, 2002, **87**, 1464–1476.
73 I. Pelah, K. Krebs and Y. Imry, Inelastic Neutron Spectra and the Vibrational Modes of the Hydrogen Layer in Alkali and Alkaline-Earth Hydroxides, *J. Chem. Phys.*, 1965, **43**, 1864–1869.
74 M. Catti, G. Ferraris, S. Hull and A. Pavese, Static Compression and H Disorder in Brucite, $Mg(OH)_2$, to 11 GPa: A Powder Neutron Diffraction Study, *Phys. Chem. Miner.*, 1995, **22**, 200–206.
75 D. Henderson and H. Gutowsky, A Nuclear Magnetic Resonance Determination of the Hydrogen Positions in $Ca(OH)_2$, *Am. Mineral.*, 1962, **47**, 1231–1251.
76 G. J. Safford and F. J. LoSacco, Study of the Low-Frequency OH^- Motions of LiOH by Neutron Inelastic Scattering, *J. Chem. Phys.*, 1966, **44**, 345–348.
77 C. J. Ridley, C. L. Bull and N. P. Funnell, Emergent Hydrogen Bonding in Dense LiOD, *Mater. Adv.*, 2022, **3**, 1673–1679.
78 S. J. Grabowski, What Is the Covalency of Hydrogen Bonding, *Chem. Rev.*, 2011, **111**, 2597–2625.
79 E. Libowitzky, Correlation of O–H Stretching Frequencies and O–H···O Hydrogen Bond Lengths in Minerals, *Monatsh. Chem.*, 1999, **130**, 1047–1059.
80 A. D. Boese, Density Functional Theory and Hydrogen Bonds: Are We There Yet, *ChemPhysChem*, 2015, **16**, 978–985.
81 M. Ernzerhof and G. E. Scuseria, Assessment of the Perdew–Burke–Ernzerhof Exchange-Correlation Functional, *J. Chem. Phys.*, 1999, **110**, 5029–5036.

